PAPER

Check for updates

Changing the reaction pathway of the CaAl₂ oxidation using ball milling†

Elias C. J. Gießelmann, [ID] Guido Kickelbick [ID] and Oliver Janka [ID] *

As previously shown, $CaAl_2$ can be oxidized using elemental O_2 to form $CaAl_2O_4$. This reaction, however, proceeds *via* $Ca_{12}Al_{14}O_{33}$ and elemental Al as intermediates which are subsequently transformed into the stoichiometric reaction product. High-energy ball milling is known to decrease the crystallite size of a material and to significantly produce defects enabling different reaction pathways compared to a highly crystalline bulk material. In this subsequent study, a different oxidizing agent (H_2O) as well as the ball milling behavior of $CaAl_2$ and the consecutive oxidation *via* elemental O_2 were studied. While the use of H_2O as the oxidizing agent showed only minor differences in the reaction products, ball milling of $CaAl_2$ decreases, as expected, the crystallite size of the material and introduces defects. This is visible both in the powder X-ray diffraction patterns and in the ^{27}Al solid-state MAS NMR spectra. In the subsequent steps, the ball milled material was oxidized in an STA system. Already 5 min of ball milling significantly changes the energy pattern of the reaction. Powder X-ray diffraction studies on the oxidized material clearly indicate that a different reaction pathway occurs. Samples ball milled for 180 min even get pyrophoric.

1. Introduction

Light weight alloys are of key importance for modern technical applications such as automotive and transportation applications,[1–5] architecture,[5–7] but also as corrosion resistant parts for air- and spacecrafts,[8–12] for medical applications like implants or stents,[10–15] or as non-sparking tools for gas stations, oil rigs or fire fighters.[16–18] In some of these alloys, intermetallic compounds play an important role.[1,5,19,20] The thermal and chemical resistance alongside astonishing mechanical properties of materials from the Ti–Al system[21] led to their use in aircraft and gas turbines.[22,23] However, the corrosion resistance of many materials is insufficient at elevated temperatures, which can be improved by alloying or special structuring.[24–26] Therefore, oxidation studies are an important field of research.[26–30] Alloys based on Ni and Al show supreme corrosion stability under extreme conditions. In AlNi for example, a protective layer of aluminum oxide Al_2O_3 (corundum, space group $R\bar{3}m$) is formed when the material is exposed to air at elevated temperatures.[31–33] Finally, aluminum alloys can be protected from oxidation by addition of small amounts of $CaAl_2$.[34]

Since intermetallic compounds are, in contrast to ionic compounds, not restricted to charge neutrality with respect to their compositions, they exhibit a plethora of different compositions and crystal structures[35] in their respective binary phase diagrams.[36] This manifold could, in theory, be utilized to synthesize valence precise *e.g.* ternary chalcogenides. Hoppe and co-workers prepared different AMO_2 phases (A = Li–K, M = In, Tl) starting from the Zintl phases NaTl, KTl, and LiIn[37–39] and also CsAuO could be obtained by the reaction of CsAu with dry O_2.[40] The oxidation of BaCu and YCu as well as related compounds led to the high-temperature superconductor $YBa_2Cu_3O_{7-\delta}$.[41–44] Jung and coworkers used different homo- and heterogeneous alloys for the synthesis of various different oxides,[45–53] but also $CaAl_2S_4$ and $SrAl_2S_4$[54] as well as Eu_2GeS_4,[55] $EuAl_2S_4$[56] and $LiGaX_2$ (X = O, S)[57] were synthesized by this route.

Recently, we have shown that the cubic Laves phase $CaAl_2$ (space group $Fd\bar{3}m$) can also be oxidized to the expected product $CaAl_2O_4$ (space group $P2_1/c$);[58] however, the reaction is far away from being straightforward. When heat-treating $CaAl_2$ under air, Ar/O_2 mixtures or elemental oxygen, initially $Ca_{12}Al_{14}O_{33}$ (mineral mayenite; space group $I\bar{4}3d$) is formed. This compound is significantly richer in calcium as the starting material, leaving unoxidized elemental aluminum behind. This was proven by X-ray diffraction and ^{27}Al NMR experiments. Repetitive grinding and oxidation finally led to almost phase pure $CaAl_2O_4$ samples. In this paper, we report a follow-up study in which a different oxidizing agent, H_2O, was used

Inorganic Solid State Chemistry, Saarland University, Campus C4.1, 66123 Saarbrücken, Germany. E-mail: oliver.janka@uni-saarland.de

to investigate the differences between water and O_2. Furthermore, it is known that ball milling can not only be used to reduce the particle and crystallite size of a material, but also to introduce defects, activating the material. This can lead to phase transitions,[59] partial reduction[59] or can be used to e.g. surface modify transition metal oxides[60,61] or to intercalate Li into activated transition metal oxides.[62,63] Therefore, the precursor $CaAl_2$ was activated via high-energy ball milling. The different reaction pathways as well as their intermediates were investigated with the help of powder X-ray diffraction experiments, ^{27}Al solid-state NMR studies, and thermal analyses.

2. Experimental

Synthesis

Precursor $CaAl_2$. Calcium pieces (ChemPur, Karlsruhe, Germany, 99.5%) and aluminum pellets (Onyxmet, Olsztyn, Poland, 99.99%) were used as received for the synthesis of the intermetallic starting material $CaAl_2$. The binary precursor was prepared on a 400–500 mg scale. The Ca pieces were stored under an argon atmosphere; surface contaminations were removed mechanically prior to use. The synthesis of the binary compounds was carried out in a custom-build arc furnace. Elements were transferred under argon into a water-cooled copper hearth and arc-melted under dried argon at 800 mbar.[64] The argon was purified prior to use with titanium sponge (873 K), silica gel, and molecular sieves. To avoid evaporation of Ca, the Al pieces were piled on top and additionally enclosed in Al foil. Careful melting created an encapsulation of the Ca pieces. The resulting bead was turned over and remelted three times to increase the homogeneity. The weight loss in all cases was <1 mass%. The as-cast samples are silver metallic; ground powders are grey and stable in air for months. Phase purity was checked by powder X-ray diffraction (vide infra).

High-energy ball milling. For ball milling small amounts of $CaAl_2$ (~1 g of material), a home built stainless steel jar (stainless steel 1.4125) with a volume of approximately 5 mL was used in a Mixer Mill, MM400 (Retsch, Haan, Germany) using one stainless steel ball (∅ = 10 mm; mass of ~4 g) and a frequency of 30 Hz for different times (5–180 min). Before each milling step 300 μL of DME (1,2-dimethoxyethane) were added to the milling jar to avoid cementation. The milling jar was loaded in an argon filled glove box (MBraun UNIlab pro eco) with H_2O and O_2 values below 0.1 and 0.5 ppm, respectively. After every milling step, the jar was transferred back to the glovebox to empty out the milling jar. The powder stuck to the walls was mechanically removed and a small portion was taken for X-ray powder diffraction and thermal analysis/oxidation in an STA system (vide infra).

Caution: Ball-milled metals and intermetallic compounds can get pyrophoric after milling. The handling of the samples under an inert atmosphere (e.g. inside an Ar filled glove box) is advised.

Oxidation of $CaAl_2$. Oxidation reactions were performed in a STA system (vide infra) and a custom-built oxidation setup using a tube furnace (Carbolite Gero GmbH & Co. KG, Neuhausen, Germany) as the heating device. Pure oxygen, as well as wet argon were used as oxidation media. The flow rate for all gases was 20 mL min^{-1}. For the wet argon, argon was bubbled through demineralized, degassed H_2O before entering the furnace. The samples were placed in porcelain boats and centered in the tube furnace.

Thermal analysis/oxidation

Simultaneous thermogravimetric analysis (TGA) and differential scanning calorimetry (DSC) were carried out with a TGA/DSC 1 Star HT/1600 system (Mettler Toledo, Columbus, OH, USA) under an Ar/O_2 atmosphere with flow rates of 40 mL min^{-1} each. For all oxidation experiments heating and cooling rates of 20 K min^{-1} and dwelling periods of 60 min were applied. Samples were placed into alumina crucibles (∅ = 6 mm, h = 4.5 mm) for the STA measurements.

Powder X-ray diffraction

Powder X-ray diffraction (PXRD) patterns of the pulverized samples were recorded at room temperature on a D8-A25-Advance diffractometer (Bruker, Karlsruhe, Germany) in Bragg Brentano θ–θ-geometry (goniometer radius 280 mm) with CuK_α-radiation (λ = 154.0596 pm). A 12 μm Ni foil working as the K_β filter and a variable divergence slit were mounted at the primary beam side. A LYNXEYE detector with 192 channels was used at the secondary beam side. Experiments were carried out in the 2θ range of 6–130° with a step size of 0.013° and a total scan time of 1 h. The recorded data was evaluated using Rietveld refinements[65,66] with the Bruker TOPAS 5.0 software,[67] the fundamental instrument parameters were determined beforehand. The crystallite sizes were determined from TOPAS using the LVol-IB values. For the ball-milled samples, the strain L parameter was refined additionally. To determine the amorphous part of a sample, ~15 mass% of elemental Si were added to the sample and homogenized. During the Rietveld analysis, the contribution of the internal standard was fixed to the weighed value, enabling the determination of an amorphous fraction where present.

SEM/EDX data

Semi-quantitative EDX analyses of one ball-milled sample of $CaAl_2$ were conducted on a JEOL 7000F (JEOL, Freising, Germany) scanning electron microscope equipped with an EDAX Genesis 2000 EDX detector (EDAX, Unterschleissheim, Germany). The sample was sprinkled on conductive carbon tape and one area scans as well as three independent data points were measured.

^{27}Al solid-state MAS NMR

^{27}Al solid-state MAS NMR spectra were recorded on an Avance III 400 WB (Bruker Biospin, Ettlingen, Germany) at 104.35 MHz using magic-angle spinning (MAS). The samples were used as fine powders. To reduce density and electrical

conductivity, samples were mixed with dried sodium chloride in a ratio of 1:9 (sample:NaCl) or higher. The diluted samples were loaded into a cylindrical ZrO_2 rotor with a diameter of 4 mm and spun at the magic angle at a frequency of 13 kHz. All experiments conducted were single-pulse experiments with a typical pulse length of 0.83 μs (≈30° pulse) and a relaxation delay of 1 s. Resonance shifts were referenced to an aqueous 1 molar $AlCl_3$ solution. The NMR spectra were recorded using the Bruker Topspin[68] software; the analysis was performed with the help of the Dmfit software.[69]

3. Results and discussion

Precursor characterization

As the starting material, the cubic Laves phase $CaAl_2$ ($MgCu_2$ type, space group $Fd\bar{3}m$, $a = 804.02(1)$ pm)[58,70] was used. It could be shown by XRD and NMR investigations that ~5 mass% of the Al richer phase $CaAl_4$ is present ($CaGa_4$ type, space group $C2/m$, $a = 616.91(1)$, $b = 618.50(1)$ $c = 634.34(1)$ pm, $\beta = 118.03(1)°$).[70] When oxidizing this compound with air or pure O_2 the structures of the main products are the ternary oxides $Ca_{12}Al_{14}O_{33}$ (mineral mayenite, own type, space group $I\bar{4}3d$, $a = 1198.2$ pm)[71] and the expected product $CaAl_2O_4$ (own type, space group $P2_1/c$, $a = 870$, $b = 809.2$, $c = 1746.9$ pm, $\beta = 119.589$).[72] Besides these two ternaries, the binary oxides CaO (NaCl type, space group $Fm\bar{3}m$, $a = 474$ pm)[73] and Al_2O_3 (own type, space group $R\bar{3}c$, $a = 486$, $c = 1324$ pm)[73] as well as two other ternary oxides $Ca_3Al_2O_6$ (own type, space group $Pa\bar{3}$, $a =$ 1526.2 pm)[74] and $CaAl_4O_7$ (own type, space group $C2/c$, $a = 1289$, $b = 888$, $c = 545$ pm, $\beta = 107.05°$)[75] have to be mentioned as important compounds that are observed during oxidation. A detailed discussion of the chemical structures of these can be found in the original literature cited above or in the previously published work.[58] Fig. 1 depicts a comparative schematic of the previously published results[58] in comparison to the outcome of this work based on the crystal structures involved.

Oxidation of $CaAl_2$ using wet argon

In a first approach of changing the outcome of the oxidation reaction of $CaAl_2$ the idea of using different oxygen sources came up. One possibility is to use water instead of oxygen in the home-built tube furnace setup. However, instead of using pure water, an argon stream was bubbled through degassed, demineralized water and fed into the furnace. The result does not show any noticeable difference to the outcome of the O_2 oxidation, with mayenite ($Ca_{12}Al_{14}O_{33}$) still being the main product. One exception might be that in contrast to small amounts of cubic $Ca_3Al_2O_6$, approximately 5 mass% of the monoclinic oxide $CaAl_4O_7$ could be identified in the powder diffraction pattern (Fig. 2; Table 1).

Ball milling experiments

In the second approach, instead of changing the oxidizing agent, milling of the powders was employed. This can be used to reduce the average crystallite size, increase the surface area of the starting material and introduce defects and amorphous regions or even induce phase transitions.[76–78] At first,
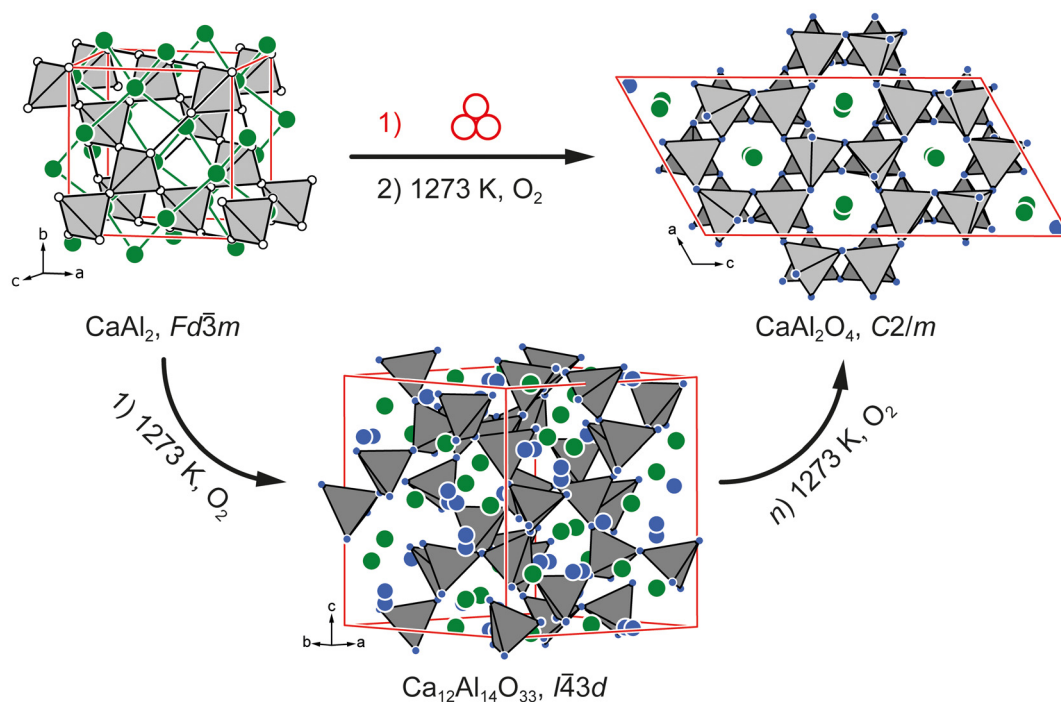

Fig. 1 Two reaction pathways for the oxidation of cubic $CaAl_2$ at 1273 K with elemental O_2. A direct formation of monoclinic $CaAl_2O_4$ is observed when activating the material by ball milling. Without ball milling, cubic $Ca_{12}Al_{14}O_{33}$ is formed initially as previously reported.[58]
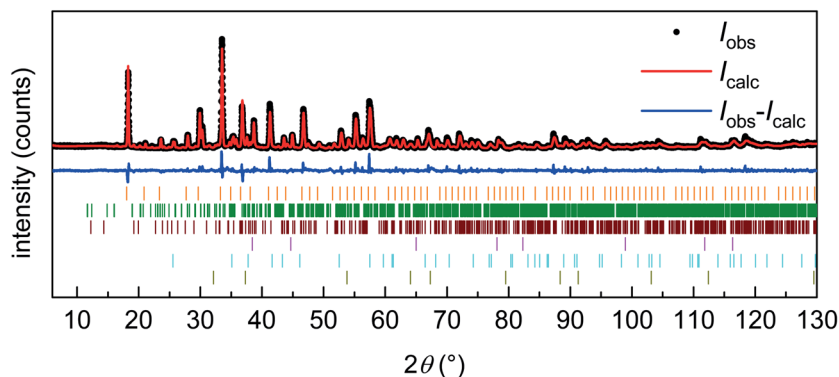
Fig. 2 Powder X-ray diffraction pattern of the oxidation product of $CaAl_2$ in a tube furnace at 1273 K for 1 h using wet argon. Experimental data are shown as black dots, the simulated diffraction pattern from refinement as the red line, the difference is shown as a continuous blue line, and the Bragg positions for $Ca_{12}Al_{14}O_{33}$, $CaAl_2O_4$, $CaAl_4O_7$, Al, Al_2O_3 and CaO are shown as orange, green, brown, pink, cyan and olive ticks.

Table 1 Phase contributions obtained by PXRD (mass%) *via* Rietveld refinement for the oxidation of $CaAl_2$ using wet argon. The standard deviations are ± 1 mass%

$Ca_{12}Al_{14}O_{33}$	$CaAl_2O_4$	$CaAl_4O_7$	CaO	Al_2O_3	Al	Fig.
63	13	10	1	8	5	S1

intermetallic $CaAl_2$ was treated in a vibrating ball mill for up to three hours. A significant decrease of the crystallite size during milling could be observed using powder X-ray diffraction. The broadening of the reflections is already visible in the comparison of the powder diffractograms shown in Fig. 3. From the diffraction data it can also be seen that no change in the crystal structures or the phase composition is observed. Fig. 4a
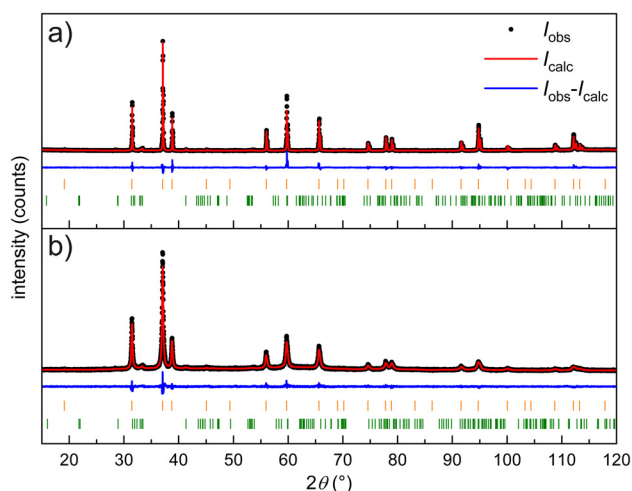

Fig. 3 Powder X-ray diffraction patterns of $CaAl_2$ as the pristine material obtained (a) after arc melting and (b) after 180 min ball milling. Experimental data are shown as black dots, the simulated diffraction pattern from refinement as the red line, the difference is shown as a continuous blue line, and the Bragg positions for $CaAl_2$ and $CaAl_4$ are shown in orange and green ticks.

illustrates the decrease of the crystallite size over time; for a second batch the crystallite sizes of the starting material and the 30 min milled material are shown. The crystallite size decreases with an almost exponential decay over the milling intervals starting from >350 nm down to roughly 50 nm after three hours (Table 2). A second batch that was milled for 30 min straight shows comparable results. The decrease in crystallite size could also be proven by ^{27}Al solid state NMR experiments. The spectra for the species milled for 90 and 180 minutes show almost identical shifts and signal shapes; only a broadening of the central transition and spinning side-bands is visible as can be seen in Fig. 4b. However, a significant effect is visible when compared to pristine $CaAl_2$.[70,79] This clearly shows that the crystallite size is reduced alongside the formation of defects leading to broadened NMR resonances. Detailed simulations of the spectra can be found in the ESI.† To verify this even further, powder X-ray diffraction experiments with known amounts of Si as the internal standard were conducted on the 30 and 180 min ball milled samples. In this way, the amorphous phase contribution can be determined. For the 30 min milled sample the amorphous phase amounts to 5(1) mass% while at 180 min 20(1) mass% are observed. Fig. S37 and S38† show the respective diffraction data along with the Rietveld fits. The sample milled for 30 min was additionally examined by SEM/EDX investigations. No abrasion of the milling jar can be observed as no Fe can be found in the EDX results.

Oxidation experiments after ball milling

To study the impact of the milling on the oxidation behavior the milled samples were transferred to an STA system. Since the transfer of the samples into the system was not possible fully under argon, the measurement was started as fast as possible. For all samples except for the one milled for 180 min, no obvious oxidation during the transfer was observed. However, for the latter, a pyrophoric behavior was observed. Powder X-ray diffraction did not show a decomposition of the starting material after 180 min of ball milling (Fig. S11†). However, since a significant amorphous contri-
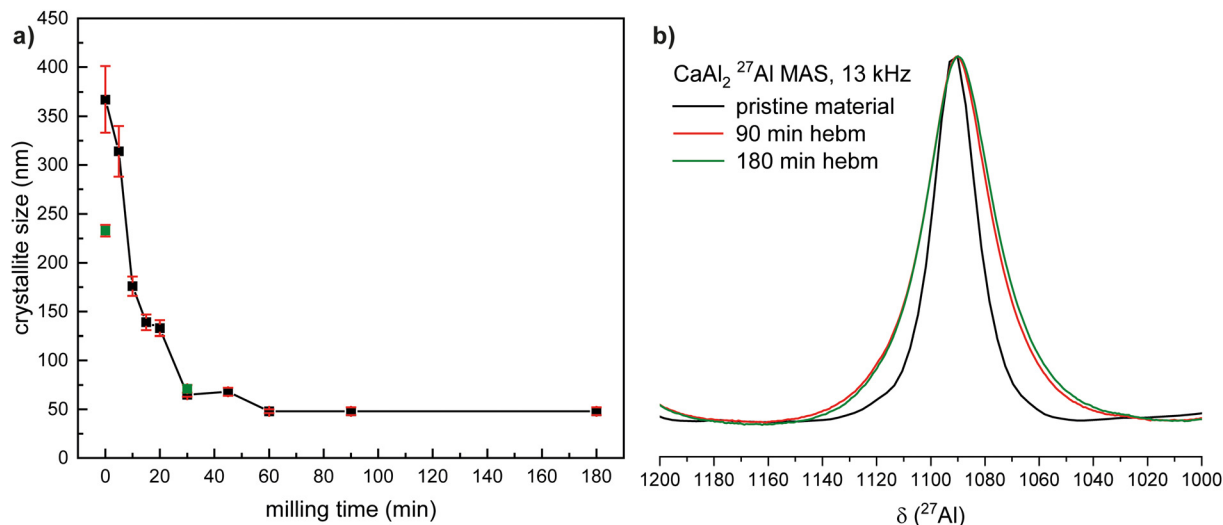
Fig. 4 (a) Decrease of the crystallite size (determined as LVol-IB) as a function of milling time, extracted from the powder diffractograms using the TOPAS software. The estimated standard deviations are indicated by error bars. The data of a second batch are shown in green. (b) ^{27}Al MAS NMR spectra for $CaAl_2$ as the pristine material (black) and after 90 and 180 minutes (red and green) of ball milling.

Table 2 Crystallite size (determined as LVol-IB) of the milled $CaAl_2$ samples at different milling times. The determined amorphous phase contributions are given

Milling time/min	Crystallite size/nm	Amorphous phase/mass%	Fig.
0	367(34)	0	S2
5	314(26)		S3
10	176(10)		S4
15	139(8)		S5
20	133(8)		S6
30	65(2)	5(1)	S7/S37
45	68(4)		S8
60	48(2)		S9
90	48(4)		S10
180	48(4)	20(1)	S11/S38

bution was deduced (*vide supra*), it is likely that the mechanochemical treatment produced a material with an increased surface area and introduced defects near/at the surface. As known for nanoparticles of ignoble metals, these are highly pyrophoric.[76–78,80–83] A similar situation could be assumed here.

Fig. 5 shows a comparison of the obtained STA data for the starting material and the milled materials after 90 and 180 minutes. For pristine $CaAl_2$, a highly exothermic reaction (Fig. 5a, red trace) at 1130 K can be observed, raising the temperature inside the STA system significantly (Fig. 5a, green trace). Furthermore, a multi-step reaction seems to take place as multiple effects are visible in the heat flux curve. In addition, a significant mass increase can be observed (Fig. 5a, black trace). The powder X-ray diffraction pattern also significantly changes. After oxidation, (Fig. 5b), several oxides can be observed, in line with what was reported previously.[58] When oxidizing the material that was ball milled for 5 min in the

STA system (Fig. S14†), an increase of $CaAl_2O_4$ can be observed right away based on powder X-ray diffraction. Fig. 5c depicts the STA results of $CaAl_2$ ball milled for 90 min. In the heat flux (red trace) it becomes evident that the heat signature becomes smeared and less intense (note that the scale bar for the heat flux is the same in all STA graphs). The overall area remains almost the same, indicating an earlier onset and an overall less pronounced reaction onset. The mass increase is a little steeper than before; however, the overall mass gain (+53 mass%) is the same for pristine and 90 min ball milled $CaAl_2$. The corresponding powder diffraction pattern is shown in Fig. 5d, indicating a different phase composition compared to the oxidized pristine material (Fig. 5b). Fig. 5e finally shows the STA results from the pyrophoric $CaAl_2$ that was ball milled for 180 min and Fig. 5f shows the corresponding powder X-ray diffraction pattern. When the sample was transferred to the STA crucible, an initial reaction was observed that stopped by itself after some seconds. It is assumed that this initial oxidation only happens on the surface and does not proceed throughout the sample, similar to what was shown for *e.g.* AlNi.[84] This assumption is strengthened by the STA results. There is still a mass increase of +42 mass%, which is, however, smaller than the one for the pristine and 90 min milled material. Finally, the amorphous phase contributions of the 30 and 180 min milled oxidized materials were determined. In both cases, the amorphous phase contribution amounts to <1 mass% (Fig. S39 and S40†).

Overall, it can be seen that with prolonged milling times, the amount of $Ca_{12}Al_{14}O_{33}$ steadily decreases while at the same time the amount of $CaAl_2O_4$ increases (Table 3). Fig. 6 depicts the evolution of the ratio between the two interesting main oxides; a plot of all phases present is shown in Fig. S36† and is given in Table 3. This observation underlines our previous assumption: Ca diffuses to the surface of the particle,
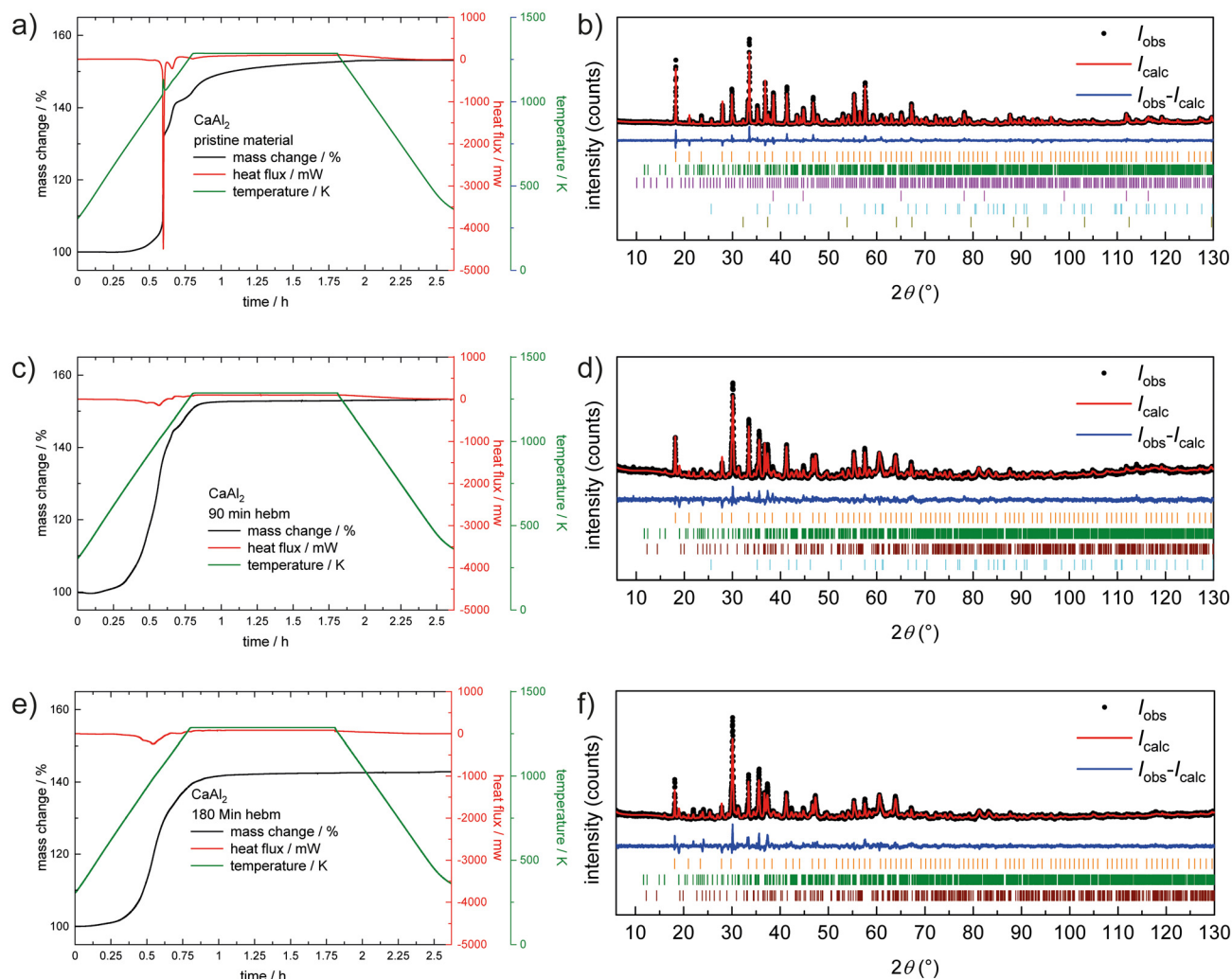
Fig. 5 STA experiments (mass change in black, heat flux in red and temperature program in green) and the corresponding Rietveld refinements of the collected powder X-ray diffraction data for the respective oxidation products of pristine (a, b) $CaAl_2$ and after 90 (c, d) and 180 (e, f) minutes ball milling. Experimental data are shown as black dots, the simulated diffraction pattern from refinement as the red line, the difference is shown as a continuous blue line, and the Bragg positions for $Ca_{12}Al_{14}O_{33}$, $CaAl_2O_4$, $Ca_3Al_2O_6$, $CaAl_4O_7$, Al, Al_2O_3 and CaO are shown as orange, green, purple, brown, pink, cyan and olive ticks.

Table 3 Results of the Rietveld refinements from powder X-ray diffraction data of the STA treated samples after different milling times. The standard deviations for the determined mass% are ±1 mass%

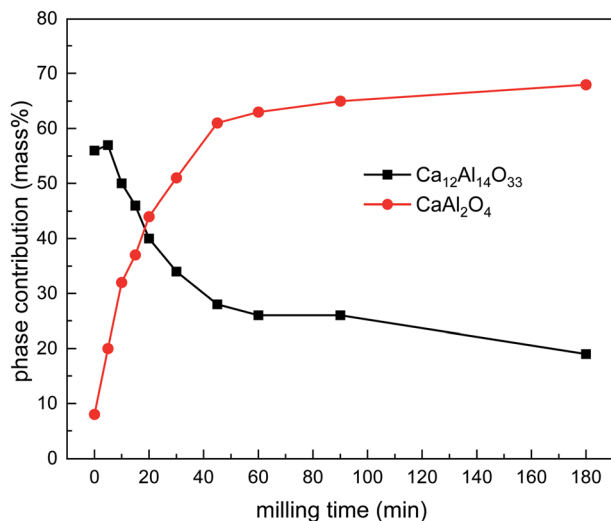| Milling time (min)	Phase contributions obtained by PXRD (mass%)							Fig.
	$Ca_{12}Al_{14}O_{33}$	$CaAl_2O_4$	$Ca_3Al_2O_6$	$CaAl_4O_7$	CaO	Al_2O_3	Al	
0	56	8	10	0	3	13	10	S13
5	57	20	4	0	0	11	8	S14
10	50	32	0	7	0	8	3	S15
15	46	37	0	7	0	7	3	S16
20	40	44	0	8	0	6	2	S17
30	34	50	0	7	0	7	2	S18
45	28	61	0	6	0	4	1	S19
60	26	63	0	8	0	3	0	S20
90	26	65	0	7	0	2	0	S21
180	19	69	0	12	0	0	0	S22

Fig. 6 Results of the Rietveld refinements of the oxidation reactions after different milling times (selected phases only). For all observed phases see Fig. S36.†

enabling the formation of $Ca_{12}Al_{14}O_{33}$ and leaving elemental Al behind.[58] When ball milling $CaAl_2$, the crystallite size gets significantly reduced, shortening the Ca diffusion path length, hampering the formation of the mayenite type structure and enabling the direct formation of $CaAl_2O_4$. This is furthermore in line with our previous quantum-chemical calculations,[58] rendering both competing oxides similar in formation energy with $CaAl_2O_4$ being the thermodynamically slightly more stable compound.

Finally, we want to address the crystallite sizes determined for the oxidized material. As shown in Fig. 4a, the crystallite size of the ball milled $CaAl_2$ steadily decreases with increasing milling time. When analyzing the crystallite sizes of the oxidized material from the STA investigations, the sample after 5 min of ball milling shows 36(3) nm for $CaAl_2O_4$ and 84(2) nm for $Ca_{12}Al_{14}O_{33}$. The crystallite sizes of $CaAl_2O_4$ roughly stay the same regardless of the applied milling time; for $Ca_{12}Al_{14}O_{33}$ an increase to ~120 nm for 10–30 min is visible followed by a decrease to ~50 nm for the 60 and 90 min milled samples. However, there is no clear trend visible in these data (Table S1†).

4. Conclusion

The intermetallic Laves phase $CaAl_2$ was oxidized in two ways: using water (in Ar) and pure O_2 after ball milling. While in the first case no difference between elemental oxygen and the un-ball milled material can be observed, the ball milled $CaAl_2$ is oxidized in a significantly different way. This can be attributed to a reduced crystallite size of $CaAl_2$ which is ~50 nm after 180 min of ball milling. Interestingly, ^{27}Al solid-state MAS NMR investigations on the milled material clearly showed that alongside the drastically reduced crystallite size also strain is

observed in the material as the NMR signals broaden. STA investigations finally confirmed that ball milling has an influence on the oxidation behavior. While the pristine un-milled sample shows an intense sharp exothermic reaction, the milled samples show a significantly broadened effect while the area of the signal is approximately the same as for pristine $CaAl_2$. Up to 90 minutes of milling all samples exhibit a similar mass gain of ~150 mass%. When $CaAl_2$ is milled for 180 min, the sample becomes pyrophoric; however, the reaction is not self-sustaining. This leads to the assumption that only the surface is oxidized as an additional mass gain is still observed in the STA experiments. The main product of the oxidation reaction of pristine $CaAl_2$ is $Ca_{12}Al_{14}O_{33}$ which crystallizes in the so called mayenite type structure. For the milled samples, the respective amount of $Ca_{12}Al_{14}O_{33}$ drops in almost an exponential fashion while instead the stochiometric oxidation product $CaAl_2O_4$ is formed in higher amounts. The presented results clearly show that already short ball milling times can significantly influence the reaction pathway and therefore drastically shift the product scope.

Author contributions

Conceptualization by GK and OJ; synthetic work by ECJG; initial draft of the manuscript by ECJG. ECJG performed the XRD, STA and ^{27}Al NMR investigations; the entire work was supervised, guided, and revised by GK and OJ. The manuscript was corrected by all authors and finalized by GK and OJ.

Data availability

Details on the Rietveld refinements, crystallite sizes, STA curves, and ^{27}Al NMR spectroscopic data can be found in the ESI.†

The data supporting this article have been included as part of the ESI.†

Conflicts of interest

The authors declare no competing interests.

Acknowledgements

References

1 F. Ostermann, *Anwendungstechnologie Aluminium*, Springer Vieweg, Berlin, Heidelberg, Germany, 2014.

2 C. Kammer, *Aluminium-Taschenbuch 1: Grundlagen und Werkstoffe*, Aluminium-Zentrale, Düsseldorf, Germany, 1995.

3 C. Jaschik, H. Haferkamp and M. Niemeyer, *in Magnesium Alloys and their Applications*, Wiley-VCH Verlag GmbH, Weinheim, Germany, 2000, pp. 41–46.

4 M. K. Kulekci, *Int. J. Adv. Des. Manuf. Technol.*, 2008, **39**, 851–865.

5 O. Janka, in *Applied Inorganic Chemistry*, ed. R. Pöttgen, T. Jüstel and C. A. Strassert, De Gruyter, Berlin, Germany, 2023, pp. 158–173.

6 Empire State Realty Trust, Empire State Building Fact Sheet, https://www.esbnyc.com/sites/default/files/esb_fact_sheet_4_9_14_14.pdf.

7 FMGB Guggenheim Bilbao Museoa, https://www.guggenheim-bilbao.eus/de/, (accessed 28.06.2023).

8 C. Veiga, J. P. Davim and A. J. R. Loureiro, *Rev. Adv. Mater. Sci.*, 2012, **32**, 14–34.

9 M. V. Ribeiro, M. R. V. Moreira and J. R. Ferreira, *J. Mater. Process. Technol.*, 2003, **143–144**, 458–463.

10 M. Peters, J. Hemptenmacher, J. Kumpfert and C. Leyens, in *Titanium and Titanium Alloys*, Wiley-VCH Verlag GmbH, Weinheim, Germany, 2003, pp. 1–36.

11 J. Barksdale, in *The encyclopedia of the chemical elements*, ed. C. A. Hampel, Reinhold Book Corp., New York, USA, 1968, pp. 732–738.

12 P. Enghag, in *Encyclopedia of the Elements: Technical Data – History – Processing – Applications*, ed. P. Enghag, Wiley VCH Verlag GmbH, Weinheim, Germany, 2004, pp. 493–509.

13 M. Peters and C. Leyens, *Titan und Titanlegierungen*, Wiley-VCH, Weinheim, Germany, 2002.

14 S. Engel and O. Janka, in *Applied Inorganic Chemistry*, ed. R. Pöttgen, T. Jüstel and C. A. Strassert, De Gruyter, 2023, pp. 255–264.

15 S. Engel and O. Janka, in *Applied Inorganic Chemistry*, ed. R. Pöttgen, T. Jüstel and C. A. Strassert, De Gruyter, 2023, pp. 265–270.

16 E. Gillam, H. P. Rooksby and L. D. Brownlee, *Acta Crystallogr.*, 1964, **17**, 762–763.

17 O. Janka and R. Pöttgen, *Z. Naturforsch., B: Chem. Sci.*, 2020, **75**, 421–439.

18 M. Buchner and O. Janka, in *Applied Inorganic Chemistry*, ed. R. Pöttgen, T. Jüstel and C. A. Strassert, De Gruyter, 2023, pp. 221–228.

19 J. R. Davis, *ASM Specialty Handbook: Aluminum and Aluminum Alloys*, ASM International, Materials Park, OH, USA, 1993.

20 D. Altenpohl, *Aluminium und Aluminiumlegierungen*, Springer, Berlin, Heidelberg, Germany, 1965.

21 P. K. Datta, H. L. Du, J. S. Burnell-Gray and R. E. Ricker, in *Corrosion: Materials*, ASM International, Materials Park, OH, USA, 2005, vol. 13B.

22 R. K. Gupta and B. Pant, in *Intermetallic Matrix Composites*, ed. R. Mitra, Woodhead Publishing, Sawston, Cambridge, England, 2018, pp. 71–93.

23 F. Appel, U. Brossmann, U. Christoph, S. Eggert, P. Janschek, U. Lorenz, J. Müllauer, M. Oehring and J. D. H. Paul, *Adv. Eng. Mater.*, 2000, **2**, 699–720.

24 C. Kenel, A. Lis, K. Dawson, M. Stiefel, C. Pecnik, J. Barras, A. Colella, C. Hauser, G. J. Tatlock, C. Leinenbach and K. Wegener, *Intermetallics*, 2017, **91**, 169–180.

25 K. Meng, K. Guo, Q. Yu, D. Miao, C. Yao, Q. Wang and T. Wang, *Corros. Sci.*, 2021, **183**, 109320.

26 P. A. Loginov, G. M. Markov, N. V. Shvyndina, G. V. Smirnov and E. A. Levashov, *Ceramics*, 2022, **5**, 389–403.

27 S. A. Kekare and P. B. Aswath, *J. Mater. Sci.*, 1997, **32**, 2485–2499.

28 Z. Li, W. Gao, Y. He and S. Li, *High Temp. Mater. Processes*, 2002, **21**, 35–46.

29 R. Pflumm, S. Friedle and M. Schütze, *Intermetallics*, 2015, **56**, 1–14.

30 A. Rahmel, M. Schütze and W. J. Quadakkers, *Mater. Corros.*, 1995, **46**, 271–285.

31 G. Geramifard, C. Gombola, P. Franke and H. J. Seifert, *Corros. Sci.*, 2020, **177**, 108956.

32 H. J. Grabke, M. W. Brumm and B. Wagemann, *Mater. Corros.*, 1996, **47**, 675–677.

33 H. Qin, X. Chen, L. Li, P. W. Sutter and G. Zhou, *Proc. Natl. Acad. Sci. U. S. A.*, 2015, **112**, E103–E109.

34 Y.-O. Yoon, S.-H. Ha, G.-Y. Yeom, H. K. Lim and S. K. Kim, in *Light Metals 2013*, Springer, Cham, Germany, 2013, pp. 323–326.

35 P. Villars and K. Cenzual, *Pearson's Crystal Data: Crystal Structure Database for Inorganic Compounds*, ASM International®, Materials Park, Ohio, USA, 2023.

36 T. B. Massalski, H. Okamoto, P. R. Subramanian and L. Kacprzak, *Binary alloy phase diagrams*, ASM International, Ohio, U.S.A., 2nd edn, 1990.

37 R. Hoppe and H.-J. Röhrborn, *Naturwissenschaften*, 1961, **48**, 453–454.

38 R. Hoppe and H.-J. Röhrborn, *Z. Anorg. Allg. Chem.*, 1964, **327**, 199–206.

39 R. Hoppe, *J. Solid State Chem.*, 1986, **65**, 127–144.

40 H. D. Wasel-Nielen and R. Hoppe, *Z. Anorg. Allg. Chem.*, 1968, **359**, 36–40.

41 P. J. Yvon, R. B. Schwarz, C. B. Pierce, L. Bernardez, A. Conners and R. Meisenheimer, *Phys. Rev. B: Condens. Matter Mater. Phys.*, 1989, **39**, 6690–6693.

42 W. Schauerte, H. U. Schuster, N. Knauf and R. Müller, *Z. Anorg. Allg. Chem.*, 1992, **616**, 186–190.

43 B. Cogel and H. U. Schuster, *Z. Anorg. Allg. Chem.*, 1993, **619**, 1765–1770.

44 H. Schuster and J. Wittrock, *J. Therm. Anal. Calorim.*, 1993, **39**, 1397–1401.

45 A. Panahandeh and W. Jung, *Z. Anorg. Allg. Chem.*, 2003, **629**, 1651–1660.

46 P. Moser, W. Jung and H. U. Schuster, *Z. Anorg. Allg. Chem.*, 1997, **623**, 1781–1785.

47 P. Moser and W. Jung, *Z. Anorg. Allg. Chem.*, 1998, **624**, 1251–1255.

48 P. Moser, H. M. Schwunck and W. Jung, *Z. Anorg. Allg. Chem.*, 1998, **624**, 1256–1261.

49 H. M. Schwunck, P. Moser and W. Jung, *Z. Anorg. Allg. Chem.*, 1998, **624**, 1262–1266.

50 H. M. Schwunck, P. Moser and W. Jung, *Z. Anorg. Allg. Chem.*, 1999, **625**, 407–410.

51 H. M. Schwunck, P. Moser and W. Jung, *Z. Anorg. Allg. Chem.*, 1999, **625**, 463–466.

52 P. Moser, V. Cirpus and W. Jung, *Z. Anorg. Allg. Chem.*, 1999, **625**, 714–718.

53 P. Moser and W. Jung, *Z. Anorg. Allg. Chem.*, 2000, **626**, 1421–1425.

54 B. Eisenmann, M. Jakowski, W. Klee and H. Schäfer, *Rev. Chim. Miner.*, 1983, **20**, 255–263.

55 M. Tampier, D. Johrendt, R. Pöttgen, G. Kotzyba, H. Trill and B. D. Mosel, *Z. Anorg. Allg. Chem.*, 2002, **628**, 1243–1245.

56 E. C. J. Gießelmann, S. Engel, S. Pohl, M. Briesenick, L. P. Rüthing, C. Kloos, A. Koldemir, L. Schumacher, J. Schmedt auf der Günne, G. Kickelbick and O. Janka, *Chem. Mater.*, 2024, DOI: 10.1021/acs.chemmater.4c02093.

57 J. Sappl, F. Jung and C. Hoch, *Chem. Mater.*, 2020, **32**, 866–873.

58 E. C. J. Gießelmann, S. Engel, J. G. Volpini, H. Huppertz, G. Kickelbick and O. Janka, *Inorg. Chem. Front.*, 2024, **11**, 286–297.

59 A. Betke and G. Kickelbick, *New J. Chem.*, 2014, **38**, 1264–1270.

60 A. Fischer, C. Ney and G. Kickelbick, *Eur. J. Inorg. Chem.*, 2013, **2013**, 5701–5707.

61 A. Betke and G. Kickelbick, *Inorganics*, 2014, **2**, 410–423.

62 D. Becker, M. Klos and G. Kickelbick, *Inorg. Chem.*, 2019, **58**, 15021–15024.

63 D. Becker, R. Haberkorn and G. Kickelbick, *Eur. J. Inorg. Chem.*, 2019, **2019**, 4835–4845.

64 R. Pöttgen, T. Gulden and A. Simon, *GIT Labor-Fachz.*, 1999, **43**, 133–136.

65 H. M. Rietveld, *Acta Crystallogr.*, 1967, **22**, 151–152.

66 H. M. Rietveld, *J. Appl. Crystallogr.*, 1969, **2**, 65–71.

67 Bruker AXS Inc., *Topas, Version 5*, Karlsruhe, Germany, 2014.

68 Bruker Corp., *Topspin*, Karlsruhe, 2008.

69 D. Massiot, F. Fayon, M. Capron, I. King, S. Le Calvé, B. Alonso, J.-O. Durand, B. Bujoli, Z. Gan and G. Hoatson, *Magn. Reson. Chem.*, 2002, **40**, 70–76.

70 S. Engel, E. C. J. Gießelmann, L. E. Schank, G. Heymann, K. Brix, R. Kautenburger, H. P. Beck and O. Janka, *Inorg. Chem.*, 2023, **62**, 4260–4271.

71 W. Büssem and A. Eitel, *Z. Kristallogr.*, 1936, **95**, 175–188.

72 W. Hörkner and H. Müller-Buschbaum, *J. Inorg. Nucl. Chem.*, 1976, **38**, 983–984.

73 W. P. Davey and E. O. Hoffman, *Phys. Rev.*, 1920, **15**, 333.

74 H. E. Swanson, N. T. Gilfrich and G. M. Ugrinic, *Natl. Bur. Stand. Circ.*, 1955, **5**, 10–13.

75 E. Boyko and L. G. Wisnyl, *Acta Crystallogr.*, 1958, **11**, 444–445.

76 H. Yang and H. Bakker, *Mater. Sci. Eng., A*, 1994, **181–182**, 1207–1211.

77 P. Baláž, M. Achimovičová, M. Baláž, P. Billik, Z. Cherkezova-Zheleva, J. M. Criado, F. Delogu, E. Dutková, E. Gaffet, F. J. Gotor, R. Kumar, I. Mitov, T. Rojac, M. Senna, A. Streletskii and K. Wieczorek-Ciurowa, *Chem. Soc. Rev.*, 2013, **42**, 7571–7637.

78 D. Tan and F. García, *Chem. Soc. Rev.*, 2019, **48**, 2274–2292.

79 C. Benndorf, H. Eckert and O. Janka, *Acc. Chem. Res.*, 2017, **50**, 1459–1467.

80 A. Egeberg, T. Block, O. Janka, O. Wenzel, D. Gerthsen, R. Pöttgen and C. Feldmann, *Small*, 2019, **15**, 1970200.

81 T. Klein, C. Pauly, F. Mücklich and G. Kickelbick, *Intermetallics*, 2020, **124**, 106851.

82 T. Klein and G. Kickelbick, *Nanotechnology*, 2020, **31**, 265605.

83 S. Riegsinger, R. Popescu, D. Gerthsen and C. Feldmann, *Chem. Commun.*, 2022, **58**, 7499–7502.

84 G. Kresse, M. Schmid, E. Napetschnig, M. Shishkin, L. Köhler and P. Varga, *Science*, 2005, **308**, 1440–1442.